CORA Cork Open Research Archive
Cartlann Taighde Oscailte Chorcaí

Title	Automatic inspection and assessment of a cross-passage twin tunnel using UAV
Authors	Zhang, Ran;Wang, Chao;Li, Zili
Publication date	2025
Original Citation	Zhang, R., Wang, C. and Li, Z. (2025) 'Automatic inspection and assessment of a cross-passage twin tunnel using UAV', Automation in Construction, 175, p.106200. DOI: 10.1016/j.autcon.2025.106200
Type of publication	Article (peer reviewed)
Link to publisher's version	10.1016/j.autcon.2025.106200
Rights	© 2025, the Author(s). Published by Elsevier B.V. This is an open access article under the CC BY license (http://creativecommons.org/licenses/by/4.0/). - https://creativecommons.org/licenses/by/4.0/
Download date	2026-11-17 09:47:21
Item downloaded from	https://hdl.handle.net/10468/17329



UCC
University College Cork, Ireland
Coláiste na hOllscoile Corcaigh

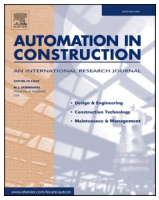
Automation in Construction 175 (2025) 106200



Contents lists available at ScienceDirect

Automation in Construction

journal homepage: www.elsevier.com/locate/autcon



Automatic inspection and assessment of a cross-passage twin tunnel using UAV

Ran Zhang [a], Chao Wang [a,b,*], Zili Li [a,b]

[a] School of Engineering and Architecture, University College Cork, Cork, Ireland
[b] Irish Centre for Research in Applied Geosciences, Science Foundation Ireland, Dublin, Ireland

ARTICLE INFO

Keywords:
Twin tunnel
Cross passage
Automatic inspection
Photogrammetry
Tunnel deformation and defects
Unmanned aerial vehicles (UAV)

ABSTRACT

The inspection of large-scale tunnel networks is essential to identify any long-term deterioration mechanisms. Traditional manual inspection is not automatic and adaptive in geometrically complex tunnel configurations. This paper presents an automatic unmanned aerial vehicle (UAV)-based tunnel assessment application in a critical cross-passage twin tunnel section of Dublin Port Tunnel. It adopts a reactive method for UAV navigation and photogrammetry, and a point cloud for data processing. This study specifically verifies the patterns of cross-section deformation and defect distribution in twin tunnels and discovers that the deterioration pattern agrees with previous monitoring results. It shows that observed tunnel deformation could be attributed to the effect of twin tunnel interaction and vehicle cross passage, whilst the distribution of lining cracks could be associated with the differential structural stiffness and the differential longitudinal bending along the tunnel section.

1. Introduction

Regular inspection of tunnel structures is essential for asset maintenance and relevant repairs to ensure structural safety and serviceability. In general, the structural health inspection of tunnels includes defects such as surface crack, concrete spalling, water leakage and drainage system blockage [1]. Traditionally, tunnels were mainly inspected by manual methods that are time-consuming, labour-intensive, subjective, and costly. The emergence of more advanced technologies, like automated robots, facilitates automatic inspection of large-scale geotechnical assets [2–4]. One of the promising robotic tools for automatic tunnel inspection and assessment is unmanned aerial vehicle (UAV), featuring low equipment cost, no installation and de-installation, non-destructive inspection, continuous measurements at structural scale, automated control and versatility of image-based data processing [5–10]. This robotic approach enables long-term subsurface structural health monitoring, facilitating the automated detection of structural damage and providing valuable insights into the deterioration mechanisms of tunnel assets. Image data acquisition is possible at a low cost (€6000 for equipment compared to €60,000 for a LiDAR inspection vehicle [11], plus high maintenance costs), together with the adaptability to different types of geotechnical assets, such as shafts, tunnels, and pipelines, as shown in Table 1. The disadvantage of UAVs is their lower accuracy (cm-level) compared to LiDAR (mm-level), which has made them a secondary inspection method in previous research.

Dublin Port Tunnel (DPT), one of Europe's longest urban road tunnels [12], comprises four distinct sections which are northern and southern cut-and-cover sections, middle bored section and one specific pipe-jacked section under the Belfast-Dublin railway, and is characterised by complex geometry, uneven illumination, and a lack of global navigation satellite system signal (GNSS). A series of surface defects have been developing on DPT linings since its opening in 2006, particularly at one vehicle cross passage (VCP) section, necessitating regular structural health condition monitoring and evaluation of this critical geotechnical asset. To enable a cost-effective, efficient and enhanced monitoring and assessment of the structural health condition of DPT, a reactive UAV-based automatic monitoring and inspection method is employed. The main limitations of the inspection condition for UAV include a lack of GNSS signal, low light, and complex geometry, rendering the precise UAV positioning and data acquisition challenging [13–15]. For example, in DPT, cross passages (pedestrian and vehicle cross passages) exist between twin tunnels to accommodate emergency requirements and aid the evacuation of tunnel users and the movement of vehicles, complicating the route planning for UAV-based automatic tunnel inspection. In addition, DPT has many facilities on its liner such as signals, signage, fire hydrants, wall-mounted loudspeakers, etc. These

* Corresponding author at: School of Engineering and Architecture, University College Cork, Cork, Ireland.
E-mail address: chao.wang@ucc.ie (C. Wang).

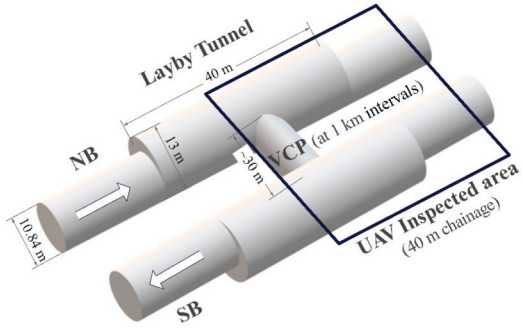
https://doi.org/10.1016/j.autcon.2025.106200
Received 19 June 2024; Received in revised form 25 March 2025; Accepted 9 April 2025
Available online 14 April 2025
0926-5805/© 2025 The Author(s). Published by Elsevier B.V. This is an open access article under the CC BY license (http://creativecommons.org/licenses/by/4.0/).

Table 1
Indicative methodology comparison among current remote sensing methods for tunnel inspection.

Methods	Accuracy & Availability	Efficiency	Cost
Manual inspection	mm-cm level; Subjective, unable to access the shaft,	Acquisition: discontinuous data (images and manual measurement) No further output	Equipment: camera (~€0.5 k); High labour cost
Specialized vehicle surveying	mm-level point cloud and cm level photos; Difficult to survey tunnel shaft	Acquisition: fast (speed in m/s) and high-quality multi-format data Processing: mature and advanced workflow	Equipment: ~ €60 k: a van (~€40 k), Sensors (cameras and LiDAR) (~€20 k); High maintenance cost
Automatic UAV inspection	cm-level photos; Adaptive for shaft, tunnel, cavern	Acquisition: slow (speed ~1 m/min) and medium- quality image data Processing: immature workflow, will require calibration and advanced algorithms to improve accuracy	Equipment cost: UAV (~€6 k); Low labour cost; Low maintenance cost (~€500 per annum)



(a) Tunnel surface defects at VCP 16 [20]



(b) Illustration of the cross-passage twin tunnel section

Fig. 1. DPT cross-passage twin tunnel section for UAV inspection.

factors restrict data collection by methods like rail cars, while UAVs can adapt to such complex environment and collect data of these facilities from multiple views. Another factor affecting UAV structural health inspection is image processing accuracy. Nevertheless, the advancement of UAV hardware and image-processing algorithms can help enhance tunnel structural health monitoring outcomes with higher definition.

To overcome the limitations and address the challenges in monitoring and inspecting DPT using UAV, this paper adopts an approach called Proximity Move-Pause-Photo for Surface Defect Inspection (PMPP-SDI) for real-time reactive control in DPT inspection tasks [11]. It enables automated tunnel surface data acquisition, and it strikes a balance between cost and performance on the DJI Mavic 2 Enterprise Dual (M2ED) platform usually used by research groups [16,17]. UAVs carry out close-range oblique photography tasks through flexible flight routines along the surface in varying cross-section geometries. The platform's non-repetitive scanning control ensures comprehensive coverage of tunnel surfaces. The UAV point cloud model generate digital surface models (DSMs) and orthomosaics in pairs, saving the efforts of data fusion of LiDAR and image data in other technologies. These outputs are useful for data segmentation and tunnel health assessment.

The UAV tunnel inspection method is applied to a cross-passage twin tunnel section of DPT to evaluate its structural health conditions. The two primary objectives of this field test include evaluating the effectiveness of the developed UAV inspection method and assessing the overall health condition of the chosen cross-passage twin tunnel section of DPT. To achieve these objectives, the paper is structured as follows: section 2 describes the tunnel conditions, UAV inspection method, and experimental setting for inspection; section 3 explains the data post-processing method, including 3D model reconstruction of the tunnel, spatial information extraction and conversion, and the generation of the defect distribution map based on orthomosaics; section 4 presents the result analysis, encompassing defect size and distribution statistics, and discussion of tunnel deformation mechanism; section 5 gives the conclusion of the paper.

2. UAV image acquisition in DPT

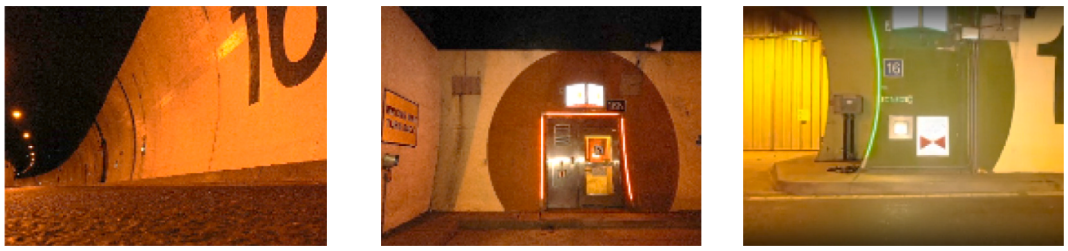
The unique challenges of DPT, such as varying tunnel geometries and low illumination conditions, require advanced navigation and imaging techniques of the UAV to ensure thorough and accurate data collection. This section introduces the inspected area and illumination conditions of DPT and discusses the UAV image acquisition method employed to effectively capture detailed images of DPT's defects and deformations.

2.1. Inspection area VCP 16

Dublin Port Tunnel, opened in 2006, serves as a key transportation infrastructure that expands a length of about 4.5 km between Dublin port and Dublin city. It has a variable tunnel periphery, ranging from 10 m to 20 m, and the tunnel includes two cut-and-cover sections, two bored sections, and one specialized pipe-jacked section under Dublin-Belfast railway [18]. DPT is structurally comprised of segmental primary lining and in-situ secondary lining and it is a dual-direction twin tunnel consisting of the Northbound Bore (NB) and the Southbound Bore (SB) [19].

The inspected section of DPT is a cross-passage twin tunnel section called VCP 16. Its lining cracking, water leakage and concrete spalling are relatively extensive, compared to other parts of the tunnel [20], as shown in Fig. 1(a). This section structurally contains bored tunnel, layby tunnel, headwall and VCP, as illustrated in Fig. 1(b). The inspection environment of the section features complex geometrical variations along tunnel alignment, posing challenges for UAV inspection route planning and so on.

The complexity of tunnel geometrical variations poses a challenge to UAV image acquisition, as shown in Fig. 2. Along bored tunnel, the circular tunnel is c.a.10 m in internal diameter. Near the start and end of the layby tunnel, there's an interior periphery change from 10 m to 13 m. Near the VCP where the twin tunnels are connected, the tunnel interior periphery achieves its maximum of 20–40 m. In this condition, the use of UAV enables image collection of 3D components with less cameras and more views in DPT than ground vehicles.



(a) Bored tunnel section (b) Diameter change at layby (c) Diameter change at VCP

Fig. 2. Illustration of complex engineering geometry of the DPT section.

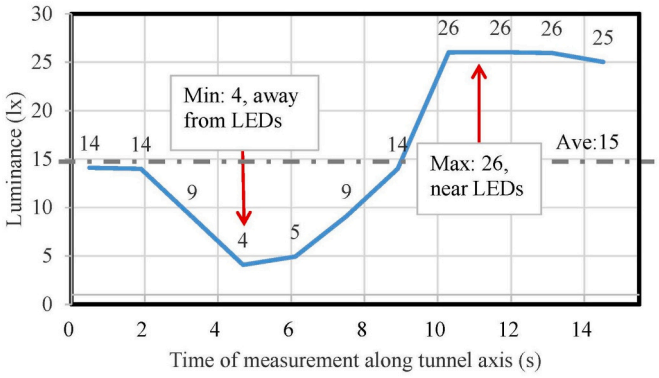


Fig. 3. Intensity variation of reflective light on tunnel side wall along DPT alignment.

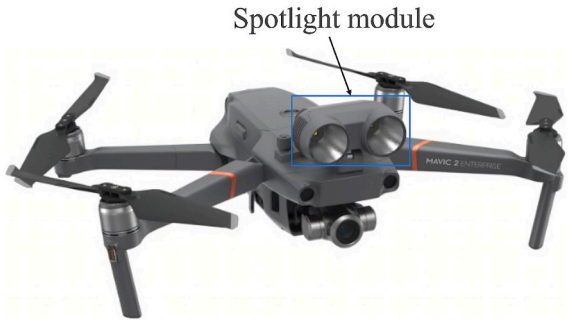


Fig. 4. UAV M2ED installed with DJI spotlight module.

2.2. Illumination conditions

In addition to its complex geometry, the DPT has low light conditions (see Fig. 3) that are unfavourable for UAV navigation. This is due to the uneven and low luminance of the LEDs in the DPT. As outlined in DJI's technical documentation, a minimum illumination level of 15 lx is necessary to ensure dependable navigation of UAVs. Therefore, the DJI spotlight module specifically designed for the M2ED model (refer to Fig. 4) has been integrated to facilitate visual navigation within the confines of tunnels. The light module is installed with a lampshade to produce even and scattering light [11]. It has a brightness of 2400 lm and can provide an adjustable light source of 300 lx in the field tests. Due to structural symmetry of DPT, the area boxed in Fig. 1(b) is chosen as the area of interest for UAV inspection where more cracks are observed compared to the opposite symmetrical section.

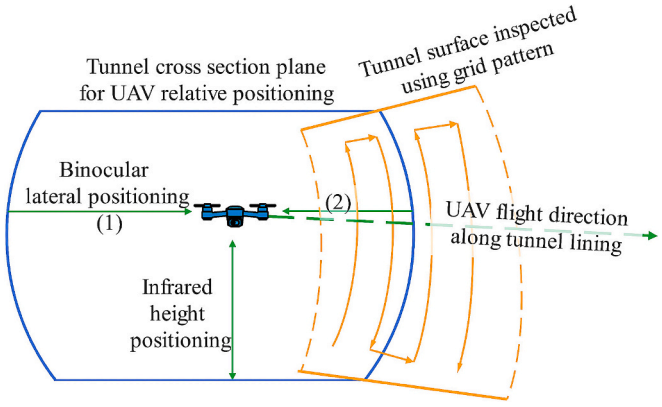


Fig. 5. Schematic of PMPP-SDI in tunnel surface information acquisition.

2.3. UAV inspection method

The PMPP-SDI real-time reactive control algorithm is built on a light weight (909 g) M2ED platform [15,16]. The M2ED is equipped with lens of DJI FC6510, which has 85° FOV, 5472 × 3078 resolution and 12 M effective pixels. Each battery allows for 22 min flight with spotlight on. An innovative method PMPP-SDI is adopted for UAV image acquisition [31]. This method is tailored for the inspection of tunnels, caverns, and shafts. Its data acquisition principle (see Fig. 5) is to use dual visual sensors' feedback to navigate a UAV along the tunnel linings and rotate gimbals for image data collection. It enables UAVs to adapt their flight path to the environmental complexity, along the surface of diameter-variant tunnel geometries. In addition, the autopilot system of a UAV maintains a constant horizontal distance between its lens and the tunnel

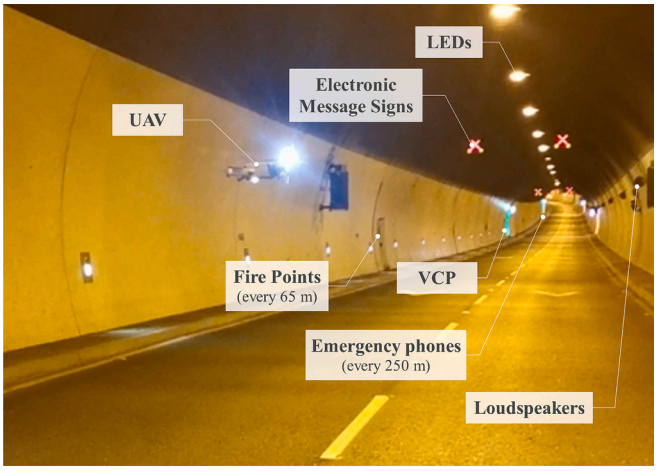


Fig. 6. Automatic UAV inspection of DPT.

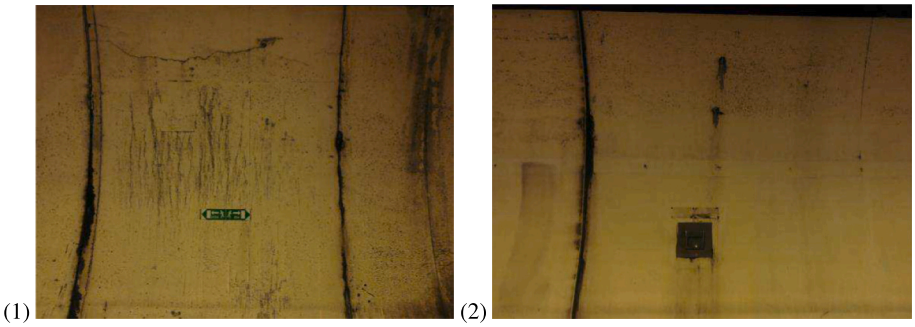


Fig. 7. Example images from raw DPT image dataset.

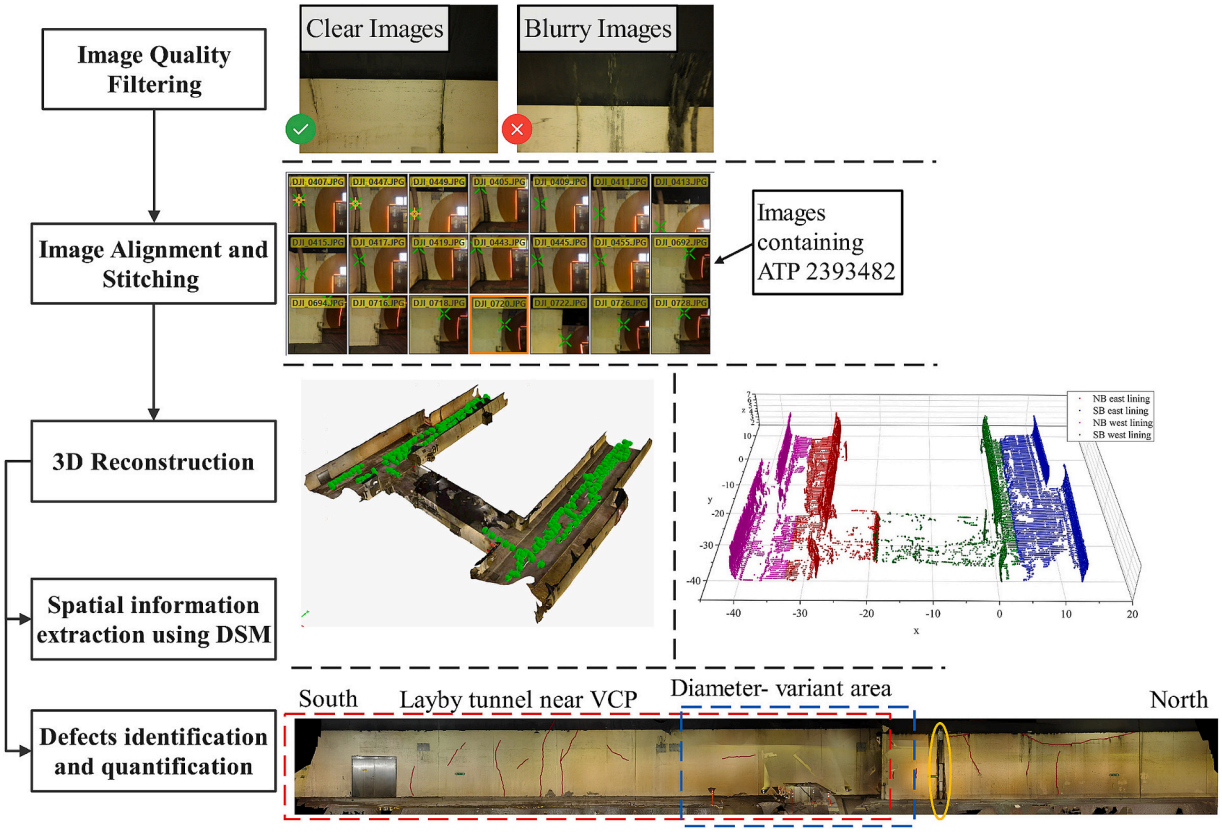


Fig. 8. Image processing workflow for DPT field test.

linings. A detailed navigation strategy is outlined in Appendix A for a UAV to follow the optimal routine. The image data is collected in a grid pattern, and the comprehensive coverage of the tunnel surface is inspected by moving the UAV along the surface and rotating the gimbal in a range [−90°, 30°] with a 60 % image overlap rate [22]. The automatic inspection allows a UAV to repeat manoeuvres at various heights inside the tunnel.

To evaluate the structural health conditions of the selected cross-passage twin tunnel section of DPT, a data processing method is employed for defect identification from PMPP-SDI. It detects abnormal colour and brightness in tunnel linings, and indicate the occurrence of cracks, water seepage in cracks or structural joints, and lining spalling. Additionally, tunnel structural deformation can be identified using digital surface models (DSM) with centimetre accuracy [21].

2.4. Research aim

The main objectives of the DPT inspection field test are to evaluate the effectiveness of the UAV inspection method and to assess the health condition of DPT twin tunnel structure. This paper firstly investigates the robustness of this navigation method in geometrically complex DPT road tunnel consisting of cross passages, layby sections, headwall, and bored section, with varying tunnel geometry. The challenge of UAV tunnel reconstruction is the close-range UAV oblique photography.

Based on surface defects and deformation analysis, the paper then aims to understand the long-term performance of the cross-passage twin tunnel section, as studies on such behaviour and the effect of VCP and twin tunnel interaction have been limited. An in-depth analysis and quantification of the tunnel defect distribution within the inspection area was carried out to provide information on defect dimensions, locations, density, and severity across the detected region.

Even though previous study has estimated the tunnel deterioration mechanism from wireless sensor network monitoring [20], an investigation is needed on continuously acquired data to give a more comprehensive picture of the tunnel long-term performance. Fig. 6 shows the onsite inspection of the tunnel section using the M2ED UAV.

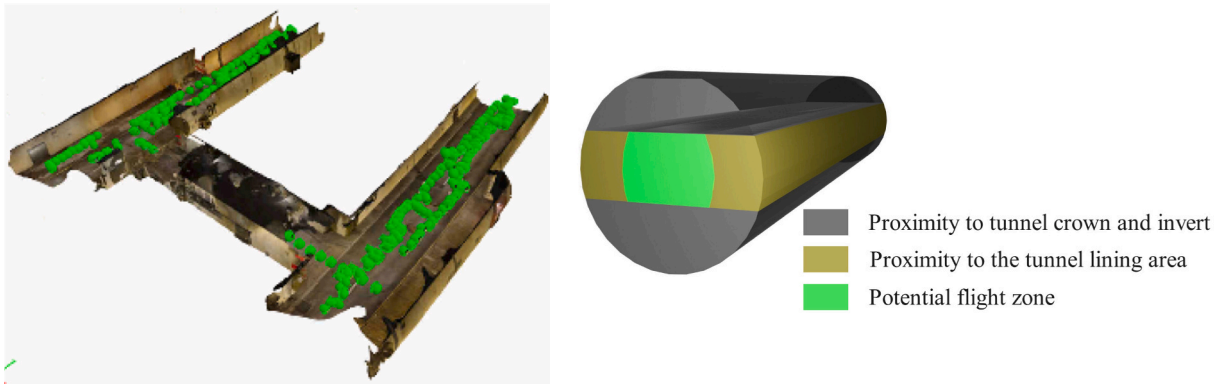


Fig. 9. Actual and target automated UAV flight trajectory in twin tunnels.

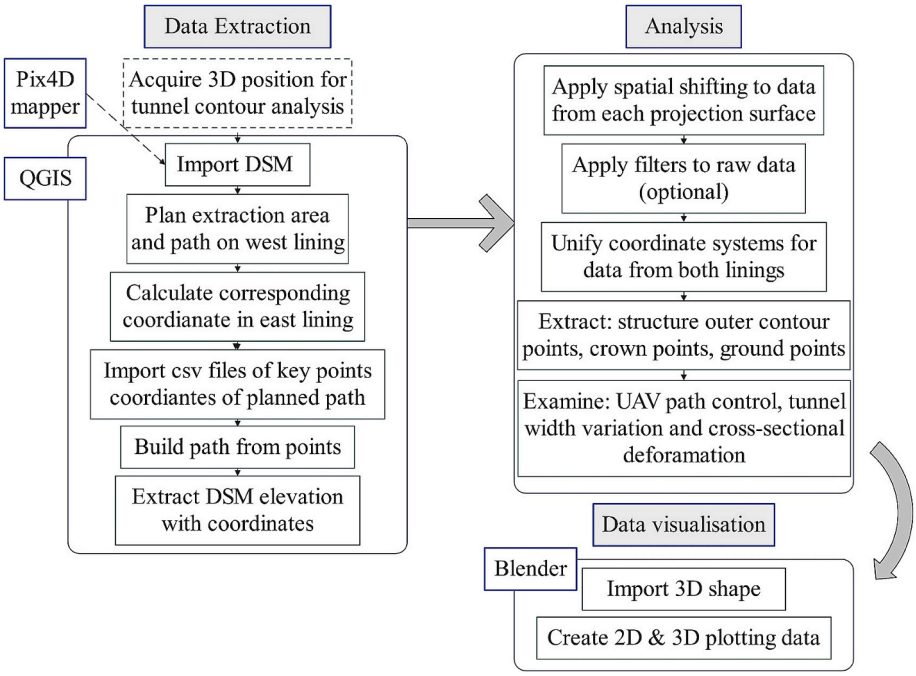


Fig. 10. Step-by-step workflow of data extraction and analysis from 3D tunnel models and software.

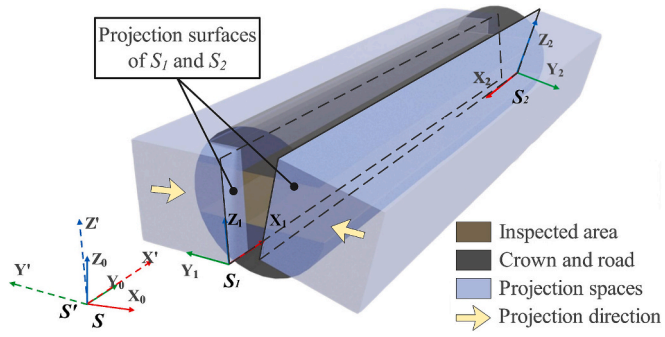


Fig. 11. Schematic of coordinate system unification (S') from DSM data (S_1,S_2) and software local (S) coordinate systems (by using the direction of S_1 and origin of S).

Two example raw images are shown in Fig. 7.

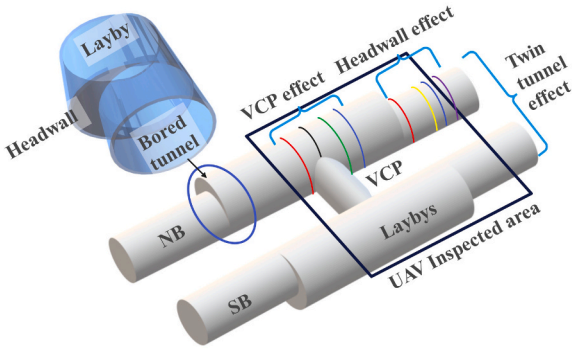
3. Methodology

This section introduces an innovative workflow for UAV point cloud analysis in tunnel inspections. 3D models are created and used for extracting spatial data to study tunnel longitudinal and cross-sectional configuration, and image data are used to study tunnel surface defect distribution.

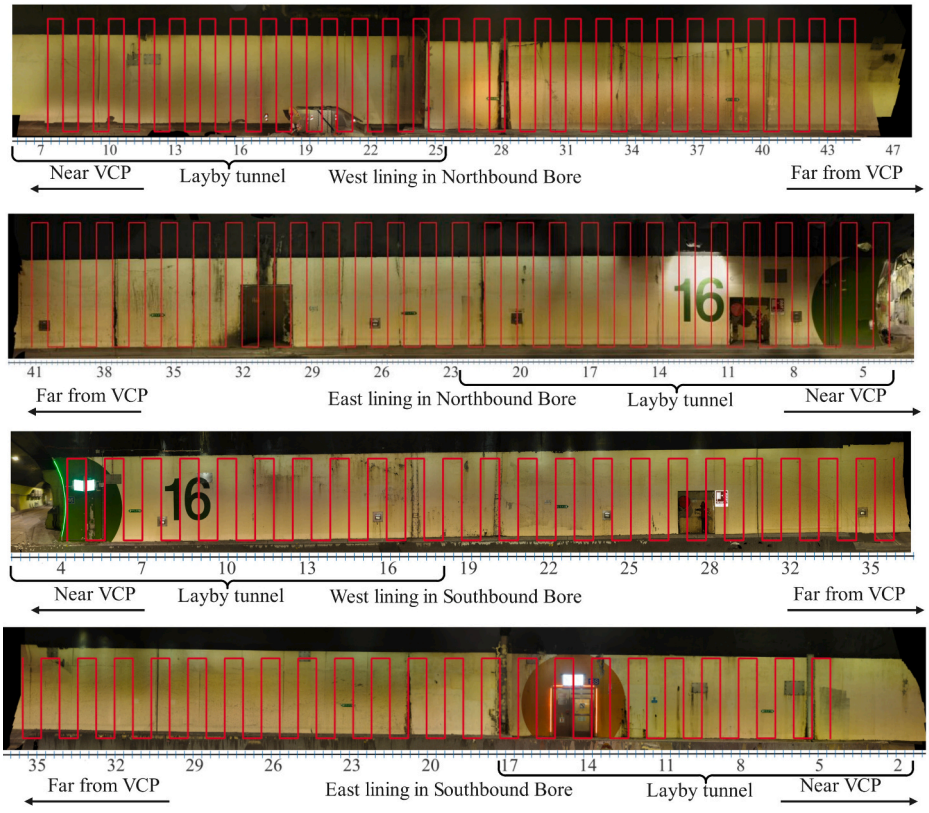
3.1. 3D reconstruction workflow

Fig. 8 illustrates the data processing workflow for 3D model reconstruction and defect analysis from a set of images using photogrammetry techniques. The method includes several key steps:

(1) Image filtering: this step involves removing images that are out of focus or have intolerable motion blurs, which can negatively



(a) Overview of data extraction at the cross-passage twin tunnel section



(b) Data extraction in four linings (tunnel mileage starts from VCP and is in the unit m)

Fig. 12. Cross-section shape extraction in DPT with extraction path in red lines. (For interpretation of the references to colour in this figure legend, the reader is referred to the web version of this article.)

impact the final 3D model's accuracy. However, UAVs can't get images without any blur under poor lighting conditions.

(2) Image stitching: this process aligns images based on common features among overlapped images. It finds the positional relationship between images and enables later spatial position calculation. As an illustration, the automatic tie point (ATP) numbered 2,393,482 is discernible in a total of 83 images.

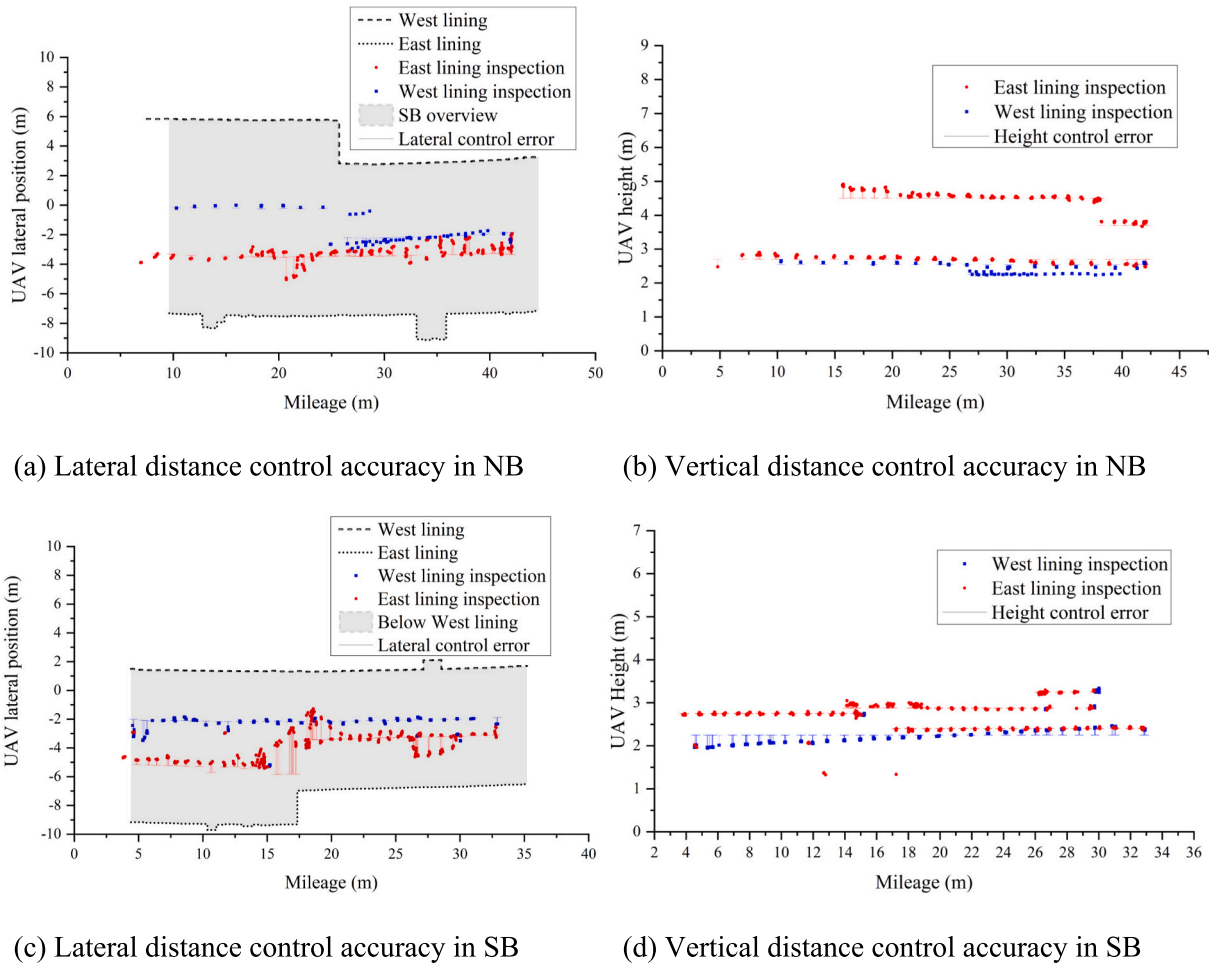
(3) 3D reconstruction is performed using Structure from Motion (SfM), with the model scale restored through proportional vectors derived from on-site global dimension measurements. The reconstructed 3D model is projected onto vertical planes to generate paired DSMs and orthomosaics. DSMs facilitate structured spatial information extraction, while orthomosaics aid in surface defect identification.

(4) Spatial information extraction using DSM: DSMs are images with depth containing spatial information of tunnel linings for structural geometry examination. It also allows UAV flight trajectory examination, using the data of camera locations and attitudes. The higher the quality of reconstruction data, the subtler dislocations this method can detect.

(5) Defect type identification and quantification: this step identifies and quantifies defects including cracks and leakages of concrete linings. This step can be achieved with manual labelling, feature-based detection, and/or machine learning techniques.

3.2. DPT spatial information extraction

The extraction of spatial information is crucial in two primary areas: analysing UAV flight trajectories for automatic control validation and



(a) Lateral distance control accuracy in NB

(b) Vertical distance control accuracy in NB

(c) Lateral distance control accuracy in SB

(d) Vertical distance control accuracy in SB

Fig. 13. UAV flying routes and control errors in the twin tunnels under coordinate system $S^{'}$.

Table 2
Navigation errors in each UAV inspection

Inspection areas	WSB	ESB	WNB	ENB	Average
Axial length of inspection	31.7 m	37.3 m	28.4 m	29.0 m	–
Standard deviation in lateral control	0.75 m	0.50 m	0.68 m	0.47 m	0.6 m
Standard deviation in height	0.06 m	0.11 m	0.23 m	0.04 m	0.1 m

assessing tunnel structural geometry. Fig. 9 qualitatively shows the UAV's flight path, which is marked by green dots, aligning with the targeted area. This efficacy of UAV automatic control is further demonstrated by the quantitative analysis of lateral and height control accuracy in tunnels. In addition, spatial information of tunnel linings is also extracted to conduct detailed analyses of tunnel geometry. This dual application of spatial information extraction not only enhances UAV flight precision in complex environments but also contributes to a comprehensive understanding of tunnel structural integrity.

The spatial information of the twin tunnel section needs to be structured within a user-defined coordinate system as the geodetic coordinate system is not applicable in global positioning system (GPS)-denied tunnels. The spatial information processing workflow is illustrated in Fig. 10. In this figure, the original tunnel lining coordinates are derived from projection in Pix4Dmapper, utilising a projection coordinate system where the projection plane is approximately parallel to the tunnel lining. Subsequently, following data selection criteria, the most representative cross-sections and tunnel contours are generated using QGIS software. Since the camera locations are in a blind coordinate system, coordinate conversion becomes essential for UAV path control and tunnel shape analysis.

The global coordinate system in Pix4Dmapper is $\boldsymbol{S}$ $(\boldsymbol{x_0}, \boldsymbol{y_0}, \boldsymbol{z_0})$ in Fig. 11. The coordinate systems of DSMs in DPT are ($\boldsymbol{S_1}$ and $\boldsymbol{S_2}$), which are the data resources. The unified spatial coordinate system $\boldsymbol{S}^{'}$ $(\boldsymbol{x}^{'},\boldsymbol{y}^{'},\boldsymbol{z}^{'})$ is created for organizing data. $\boldsymbol{S}^{'}$ share the same positive direction of $\boldsymbol{S_1}$ and the origin of $\boldsymbol{S}$. The spatial extraction of tunnel linings and cameras enables quantification of UAV control accuracy.

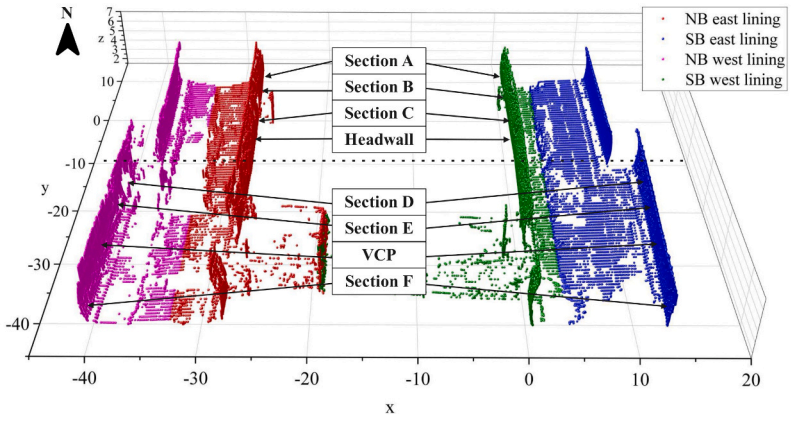
The UAV's spatial position is converted from $\boldsymbol{S}$ to $\boldsymbol{S}^{'}$. UAV's position $\boldsymbol{tc}^{'}$ in $\boldsymbol{S_1}$ is calculated using the following eq. (1):

$$\boldsymbol{tc}^{'} = (\boldsymbol{tc} - \boldsymbol{a_1})\,\boldsymbol{R_1} \tag{1}$$

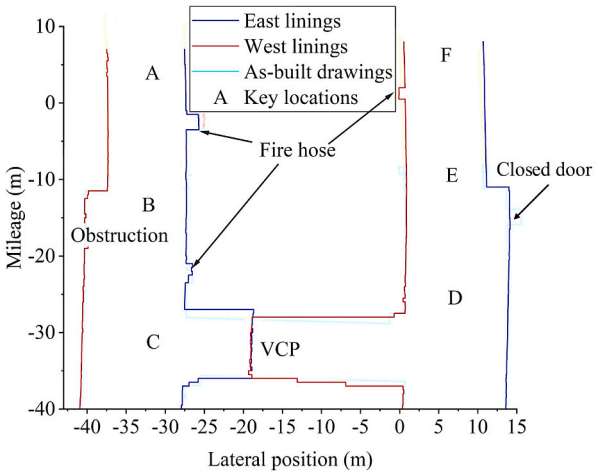
where UAV's position is $\boldsymbol{tc}$ $(\boldsymbol{x_0},\boldsymbol{y_0},\boldsymbol{z_0})$ in $\boldsymbol{S}$, and the orientation is camera rotation $\boldsymbol{Rc}$ [3 × 3]. $\boldsymbol{a_1}$ is the origins' coordinate difference between $\boldsymbol{S_1}$ and $\boldsymbol{S}^{'}$ and $\boldsymbol{R_1}$ is the rotation matrix from $\boldsymbol{S}$ to $\boldsymbol{S}^{'}$. The rotation matrix $\boldsymbol{R_i}$ could be expressed using yaw ($\boldsymbol{\theta z}$), pitch ($\boldsymbol{\theta x}$), and roll ($\boldsymbol{\theta y}$) in eq. (2):

$$\begin{aligned}\boldsymbol{R_i} &= \boldsymbol{R_z}(\boldsymbol{\theta_z})\,\boldsymbol{R_x}(\boldsymbol{\theta_x})\,\boldsymbol{R_y}(\boldsymbol{\theta_y}) \\ &= \begin{bmatrix}\cos(\theta_z) & -\sin(\theta_z) & 0\\ \sin(\theta_z) & \cos(\theta_z) & 0\\ 0 & 0 & 1\end{bmatrix}\begin{bmatrix}1 & 0 & 0\\ 0 & \cos(\theta_x) & -\sin(\theta_x)\\ 0 & \sin(\theta_x) & \cos(\theta_x)\end{bmatrix}\begin{bmatrix}\cos(\theta_y) & 0 & -\sin(\theta_y)\\ 0 & 1 & 0\\ \sin(\theta_y) & 0 & \cos(\theta_y)\end{bmatrix}\end{aligned} \tag{2}$$

In each bore, the west lining coordinates are $\boldsymbol{tp_w}$, and the east lining coordinates are $\boldsymbol{tp_e}$. They are in the form of ($\boldsymbol{x}$, $-$ ***elevation***, $\boldsymbol{y}$). Their spatial position $\boldsymbol{tp}^{'}$ in $\boldsymbol{S}^{'}$ is calculated using eq. (3):



(a) 3D overview of extracted coordinates (m) with key cross section extraction locations



(b) Comparison of tunnel top view from DSM and as-built drawing

Fig. 14. Spatial information extraction results of DPT inspection

Table 3
Interior periphery comparison at key locations of twin tunnels (/m) at around 1.6 m height

Tunnel bores	Location	Laser rangefinder	Digital model	Error
NB	A (near start)	10.25	10.07	−1.76 %
	B (start of layby)	13.30	13.43	0.98 %
	C (near VCP)	21.87	21.99	0.55 %
	D (near VCP)	13.24	13.17	−0.53 %
SB	E (end of layby)	10.31	10.25	−0.58 %
	F (near end)	10.13	10.16	0.29 %

$$\begin{cases} \boldsymbol{b}_i' = \boldsymbol{a}_i' - \boldsymbol{a}_i' \bullet \boldsymbol{n}_x' \\ \boldsymbol{tp}_w' = \boldsymbol{tp}_w + \boldsymbol{R}_1 \bullet \boldsymbol{b}_1' \\ \boldsymbol{tp}_e' = \boldsymbol{R}_{21}\ \boldsymbol{tp}_e + \boldsymbol{R}_1 \bullet \boldsymbol{b}_2' \end{cases} \tag{3}$$

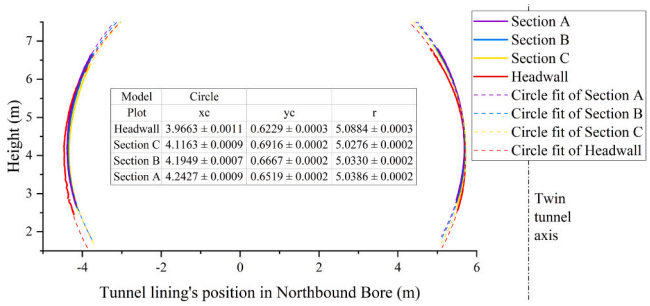
where $\boldsymbol{a}_i' = (x_i, y_i, z_i)$ is the deviation between $\boldsymbol{S}_i$ and $\boldsymbol{S}^*$, and $\boldsymbol{n}_x'$ is the x vector of this coordinate system, and $\boldsymbol{b}_i'$ is the projection of $\boldsymbol{a}_i'$ on tunnel cross-sections.

The data extraction process is depicted in Fig. 12. To study the potential deformation patterns under the influence of VCP, twin tunnel and headwall, 8 cross sections per bore are compared, as demonstrated in Fig. 12(a). The selection of cross sections avoids structural abnormalities such as firehose and sump control panel. To obtain a comprehensive representation of the geometry across the entire inspection length, cross-sectional contours are extracted at 0.75-m intervals, as illustrated by the red line in Fig. 12(b). The tunnel extraction path is a bundle of cross sections in the vertical direction connected by 0.75 m horizontal connections end to end.

3.3. UAV navigation examination

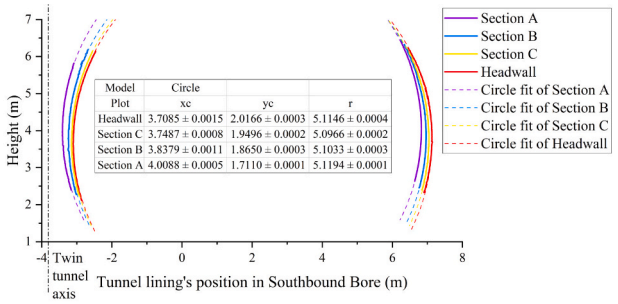
This section examines UAV navigation in tunnels by comparing the actual flight route and altitude with the expected ones, based on similar research effort in UAV road and bridge inspection [23]. UAV lateral control accuracy is examined in Fig. 13(a) and (c) and vertical control accuracy examined in Fig. 13(b) and (d) in a series of flights. The lateral control should keep constant flying distance to tunnel lining and ground, where several heights are chosen for 3D reconstruction in multiple views. In Fig. 13, the dots represent the camera's locations, and the error bars show the deviation to the expected examination distance to the tunnel surface. Analyses were made after removal of some outliers due to structural indentation, take-off action and manual supplementary photography.

The UAV has a tolerable standard deviation of 0.6 m in lateral control and 0.1 m in height (as shown in Table 2). These minor errors highlight the effectiveness of UAV inspection in GPS-denied environments with varying tunnel geometries along the alignment. Occasional irreversible



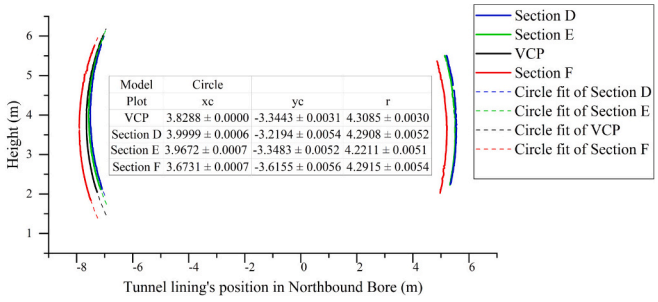
Model	Circle		
Plot	xc	yc	r
Headwall	3.9663 ± 0.0011	0.6229 ± 0.0003	5.0884 ± 0.0003
Section C	4.1163 ± 0.0009	0.6916 ± 0.0002	5.0276 ± 0.0002
Section B	4.1949 ± 0.0007	0.6667 ± 0.0002	5.0330 ± 0.0002
Section A	4.2427 ± 0.0009	0.6519 ± 0.0002	5.0386 ± 0.0002

(a) Circular tunnels cross section comparison in NB



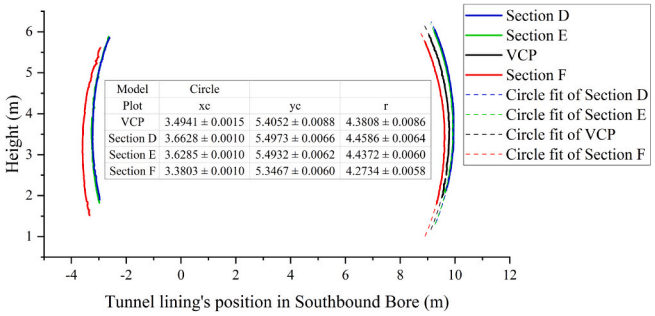
Model	Circle		
Plot	xc	yc	r
Headwall	3.7085 ± 0.0015	2.0166 ± 0.0003	5.1146 ± 0.0004
Section C	3.7487 ± 0.0008	1.9496 ± 0.0002	5.0966 ± 0.0002
Section B	3.8379 ± 0.0011	1.8650 ± 0.0003	5.1033 ± 0.0003
Section A	4.0088 ± 0.0005	1.7110 ± 0.0001	5.1194 ± 0.0001

(b) Circular tunnels cross section comparison in SB



Model	Circle		
Plot	xc	yc	r
VCP	3.8288 ± 0.0000	-3.3443 ± 0.0031	4.3085 ± 0.0030
Section D	3.9999 ± 0.0006	-3.2194 ± 0.0054	4.2908 ± 0.0052
Section E	3.9672 ± 0.0007	-3.3483 ± 0.0052	4.2211 ± 0.0051
Section F	3.6731 ± 0.0007	-3.6155 ± 0.0056	4.2915 ± 0.0054

(c) Layby tunnels cross section comparison in NB



Model	Circle		
Plot	xc	yc	r
VCP	3.4941 ± 0.0015	5.4052 ± 0.0088	4.3808 ± 0.0086
Section D	3.6628 ± 0.0010	5.4973 ± 0.0066	4.4586 ± 0.0064
Section E	3.6285 ± 0.0010	5.4932 ± 0.0062	4.4372 ± 0.0060
Section F	3.3803 ± 0.0010	5.3467 ± 0.0060	4.2734 ± 0.0058

(d) Layby tunnels cross section comparison in SB

Fig. 15. Cross-sectional spatial information extraction and comparison

control errors occurred near structural and lighting complexes. In the diameter-variant sections of the layby tunnel (Fig. 13(c)), the inspection had to be restarted, likely due to air turbulence generated by the headwalls. The height control errors are associated with the infrared sensor error. Further improvements could be made using advanced sensors and image processing techniques.

4. Tunnel health condition assessment

This section aims to assess the tunnel condition from extracted data. It first analyses the deformation of the tunnel cross sections under the potential influence of VCP, headwall and twin tunnel interaction, followed by using image analysis to obtain the distribution of surface defects and to investigate the degradation mechanisms behind the observations.

4.1. DPT spatial information

This section presents the spatial information extracted from UAV images for DPT, featuring an analysis of the tunnel's internal geometry through DSMs and comparing them with as-built drawings to evaluate the accuracy of the reconstruction. In addition, it also discusses DPT's cross-sectional deformations, focusing on the influence of the VCP and twin tunnel interaction.

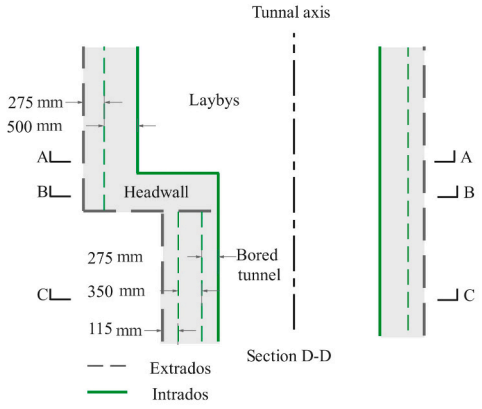
4.1.1. Observations from top view

DSMs from UAV images offer a cheap and spatially continuous way for location monitoring. Fig. 14(a) gives the extracted spatial locations of all linings presented in the same coordinate system. The top view of internal periphery of the twin tunnel is shown in Fig. 14(b) where the twin tunnel curvatures generated from the DSMs in both bores are shown. It can be seen the generated tunnel internal periphery agrees well with the as-built drawings of DPT alignment in the background.

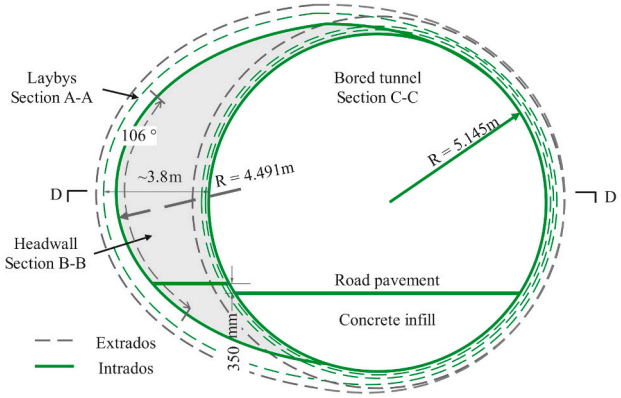
To verify the 3D model reconstruction accuracy, the measurements of the internal periphery from the reconstructed model were compared to laser rangefinder (model RS PRO RSLDM-100H with ±1.5 mm accuracy) measurement at a series of key locations, as illustrated in Fig. 14 (b). Table 3 presents the comparison between these two sets of data. Upon reviewing the comparative data, it appears that the reconstruction accuracy meets the requirements for deformation analysis. There are noticeable errors near the west lining of the layby tunnel of NB, likely due to obstructions close to the tunnel's interior walls. The blocking of drone camera by this obstruction affects the modelling of tunnel linings with flights at different heights. In different flights, various obstacles at different locations and viewpoints also led to some environmental uncertainties resulting in unpredictable noises.

4.1.2. Cross-sectional deformation

Figure 15 presents the spatial information extractions of the cross-



(a) Dimensions of tunnel linings near headwall (top view)



(b) Dimensions of cross sections and tunnel diameters (side view)

Fig. 16. Schematic of layby and bored tunnel geometry

Table 4
Comparison of radius of the fitted tunnel linings

Group	Fitted radius at marked cross-sections (m)			
Bored tunnel (Internal radius $R = 5.145$ m)	Headwall	Section C	Section B	Section A
	5.09 (NB)	5.03	5.03	5.04
	5.11 (SB)	5.10	5.10	5.12
Layby tunnel (Outer radius $R = 4.491$ m)	VCP	Section F	Section E	Section D
	4.31 (NB)	4.29	4.22	4.29
	4.38 (SB)	4.27	4.25	4.26

sections marked in Fig. 14(a) for tunnel transverse deformation investigation. The noise elimination and smoothing are optimized from computation in Pix4Dmapper. Using blurry and under-lit tunnel images, image processing achieves superior results with a small 1/4 image scale and a large (9 × 9) sliding window.

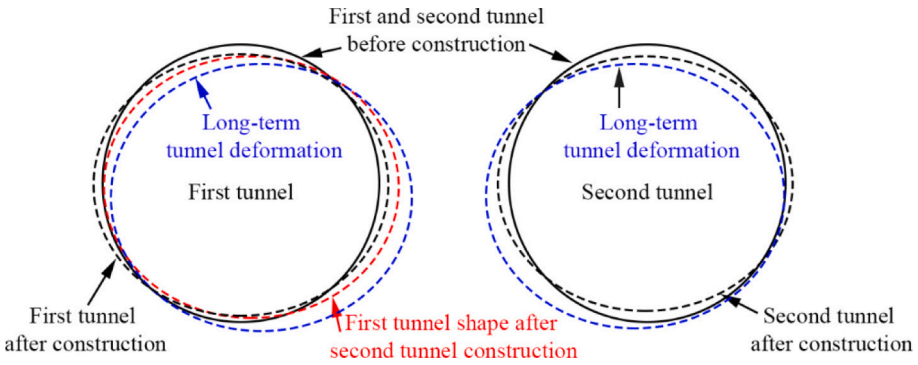
According to the technical as-built drawings of DPT in Fig. 16, the bored tunnel is circular with a radius of 5.145 m. The layby tunnel is multi-centre circular, whose inner lining circle has a 5.145 m radius, and the outer circle has a 4.491 m radius. Thus, cross-sectional contours of bored tunnels and outer lining contour of layby tunnels, generated by DSMs, were fitted in circles in Fig. 15, along with the fitting details.

The radii of the fitted circles of the selected cross sections are given in Fig. 15, and the comparison between the generated radius and the as-built radius of the tunnel sections is given in Table 4. Generally, the reconstruction reproduces the geometry of the tunnel linings with satisfactory accuracy. The reconstruction accuracy of the cross sections is in millimetres and the deviation between inner width of measured and fitted cross sections are in centimetres' level. The error may be due to noise clusters during image acquisition and processing, which create uneven surface extractions. It may also be due to lack of calibration, which can be improved with geofencing data.

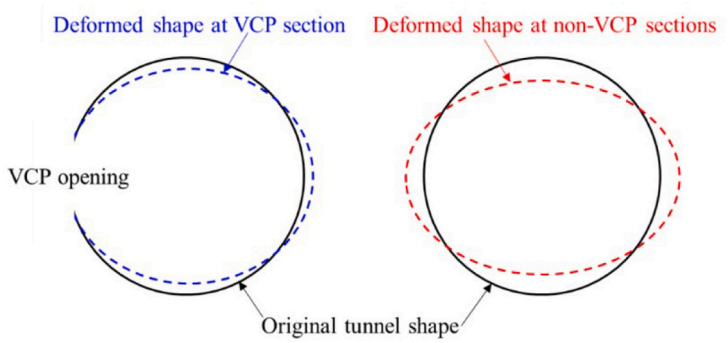
When comparing the as-built and generated bored tunnel contours at the marked sections, the fitted headwall section had a radius several millimetres to centimetres larger than the average radius of the three northern bored tunnel sections (Section A, Section B, Section C). This can be attributed to the higher stiffness at the headwall cross section that limits the development of its cross-sectional deformation. Regarding the contour comparison between as-built and fitted layby sections, the layby sections are all compressed towards the twin tunnel centreline, in consistency with the twin tunnel effect previously concluded and illustrated in Fig. 17(a) [20]. In addition, the fitted radius of the VCP section is greater than the fitted radius at other sections (Section D, Section E and Section F), indicating that the VCP section may have experienced smaller compression compared to other sections. The observation corresponds to the VCP effect summarised in previous research [20,24] that the small compression at the layby section close to the VCP can be ascribed to the horizontal pushback from VCP, as demonstrated in Fig. 17(b).

4.2. DPT surface defects

The orthomosaics have coloured textures for defect identification and tunnel surface inspection. Besides, UAV orthomosaics and DSMs are generated in pairs. It enables UAV for quantifiable defects detection, while researchers using LiDAR and cameras need to fuse the data to



(a) Tunnel deformation under twin tunnel effect ([20])



(b) Tunnel deformation under VCP effect (modified from [24])

Fig. 17. Twin tunnel effect and VCP effect



Fig. 18. 3D model of inspected DPT section (with VCP and layby tunnels)

achieve the same [25–27]. The efficiency of image processing also continues to improve with the development of algorithms [28]. Due to the advantages, this section focuses on UAV tunnel defect identification process and challenges, as well as giving details of tunnel deterioration patterns from the observations.

4.2.1. Orthomosaic accuracy

The 3D visualization of the obtained tunnel model is shown in Fig. 18. Previous studies have analysed the accuracy of 3D UAV model reconstruction. In some studies, a resolution of 0.2 mm/pixel for static images was adopted for tunnel lining inspections [28]; and another has a resolution of 20–30 mm/pixel for UAV stitched images for road pavement crack identification [17]. Another UAV reconstruction quality assessment metric is defect reflection level index, such as the metric 'pavement condition index' (PCI) for highway surface assessment [29,30]. This index gives defect identification results along with confidence levels, allowing for a more detailed inspection if larger unified dataset is generated in further inspections [31].

The orthomosaics in this paper have a resolution of 1.4 mm/pixel, which is satisfactory for the identification and quantification of cracks in DPT. Such resolution is able to locate medium and major cracks (with width greater than 3 mm) [32] and water leakage that affect the structural health. The cracks and water leakage features are generally well recorded in orthomosaics, as these defects are usually continuous along their length, and the cracks appear larger than their actual width due to salt deposits from water leakage around them.

On the other hand, some cracks within a few millimetres may not be detectable, as their width is below the resolution of 1.4 mm/pixel of the orthomosaics. Nevertheless, these small cracks are usually of less engineering concern in practice compared to large cracks over several centimetres and potentially along the water leakage and other defects.

4.2.2. DPT lining defect types

In general, tunnel structural health condition assessment includes inspection on lining cracks, spalling, and water leakage. Identifying and analysing these defect types and their distribution can be useful for both structural health assessment and long-term monitoring. Based on the approach described in section 3.2, the orthomosaics of the four tunnel sidewalls at the selected twin tunnel section are generated and displayed in Fig. 19. In the post-processing phase, the locations of all cracks, leakage and spalling were marked out in red, yellow and purple respectively. Blue rectangles are marked as diameter-variant area where headwall connects layby and bored tunnel, while red rectangles correspond to all layby areas. Table 5 shows the defect types and distributions in the selected section of DPT. Fig. 19(a) illustrated the presence of numerous cracks in the central area of the layby enlargement on NB west lining, while the diameter variant area where the headwall is located

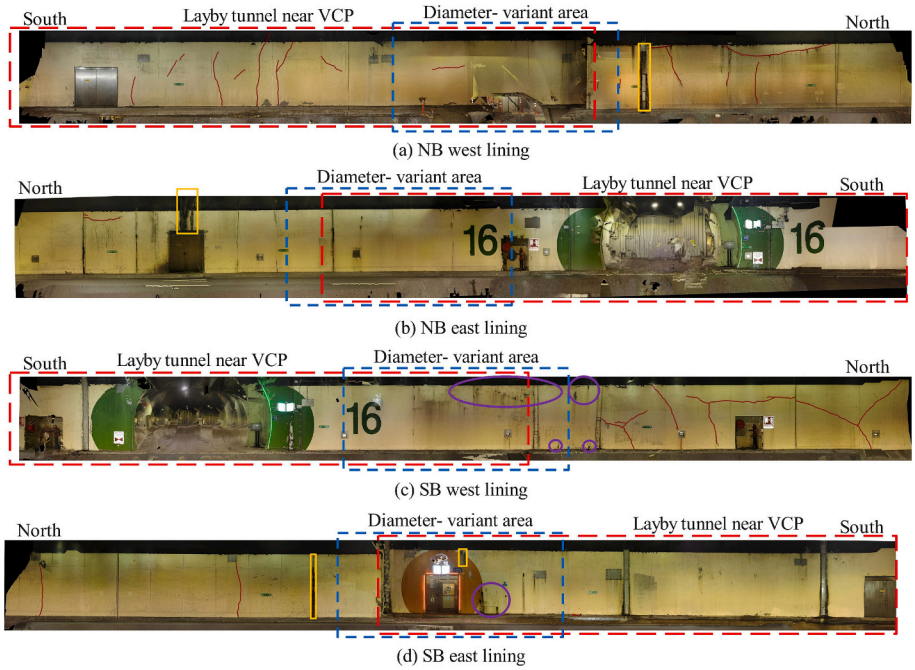
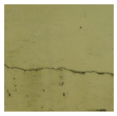
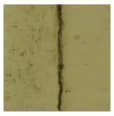


Fig. 19. Defect identification in the DSM from UAV images

Table 5
Defect patterns in the selected section of DPT

Defect	Images	Locations	Defect	Images	Locations
Horizontal cracks		- Middle of the tunnel side wall - Away from VCP	Vertical cracks		- From the tunnel shoulder to the foot
Diagonal cracks		- At various heights - Away from VCP	Water ingress		Tunnel shoulder main/along construction joint.

shows almost no cracks. Leakage was observed on NB west linings at positive drains in the bored tunnels. Fig. 19(b) shows that NB east lining exhibited minimal cracks, while the layby area exhibited slight leakage, which is distant from the VCP. In Fig. 19(c), cracks were observed at the section away from the VCP. Similarly, Fig. 19(d) shows water leakage at positive drains and some vertical cracks at the north side of the SB east lining. As spalling may merely be a secondary effect of cracks and water seepage, and analysing it requires more complex methods than visual inspection, its role in lining degradation was not considered in the preliminary analysis presented below.

4.2.3. Quantification of cracks

The impact of cracks is typically influenced by a number of factors, including their orientation, depth, development stage and location. The assessment of crack severity, particularly in the presence of salt deposits, remains a challenging aspect of structural analysis. While the width of cracks can give an indication of their potential severity, it is not a definitive indicator. In this context, the presence of cracks greater than 2.5 mm in width is often considered a structural concern. The cracks observed in the orthomosaics have a crack width that affects the structural health. Therefore, analysis of their distribution is also valuable. Although the impact of cracks can't be measured directly, this research shows a deterioration sequence of different tunnel locations in relation to the crack occurrence, which provides a useful basis for prioritising maintenance.

Table 6 presents the quantification of two major defects (cracks and water leakage), with their number and size. Major cracks range in length from around 0.85 m to 7.2 m. Defect identification and quantification was done by pixel count of the defect area in the orthomosaics. According to the the technical drawings of DPT, the curvature of the modelled surface is 1/5.145 m for the bored section or 1/4.956 m for the layby section, over a 4 m- height. Upon calculation, it was determined that long vertical cracks (exceeding 2 m in length) in the orthomosaics can represent a minimum of 97.1 % ($= r \cdot \sin(2\theta)/(r \cdot \theta)$) of the actual inspected length on a curved surface (where θ denotes the central angle corresponding to the arc). In contrast, a shorter vertical crack measuring 0.84 m can accurately reflect 99.5 % at the center height. For the long diagonal cracks, the relative error is even smaller and thus considered negligible in the statistical analysis using orthomosaics. The situation is similar for water leakage.

Figure 19 presents observations that verify the previous finding on the local deterioration patterns of tunnels. The number of cracks observed in diameter-variant areas is notably lower than in other areas, indicating that these areas exhibit greater resistance to deformation.

Table 6
Quantification of tunnel defects on orthomosaics ("width and length" refers to the horizontal and vertical dimensions of the tightest rectangular enclosure for water leakages)

Defect type		Location	Length / area (width× length)
Major cracks	Vertical cracks	NB west lining	3.78 m, 2.26 m, 2.09 m (layby); 0.84 m, 3.33 m 3.21 m (bored)
	Diagonal cracks		2.16 m, 1.26 m (layby); 2.71 m (bored)
	Horizontal cracks		2.14 m (layby); 1.92 m, 7.13 m (bored)
	Horizontal crack	NB east lining	2.40 m
	Horizontal cracks	SB west lining	1.44 m, 5.43 m
	Diagonal cracks		2.13 m, 1.81 m, 2.73 m, 4.14 m, 2.84 m
	Vertical crack		1.82 m
	Vertical crack	SB east lining	2.24 m, 2.46 m (bored)
Water leakage		NB west lining	0.82 m × 1.97 m
		NB east lining	1.07 m × 2.33 m
		SB east lining	0.26 m × 2.69 m, 0.41 m × 0.67 m, 0.35 m× 0.84 m

This is attributed to the structural stiffness provided by the headwall, which connects the bored tunnel to the layby tunnel (see grey area in Fig. 16, with a thickness of 2 m).

Figure 19(a) shows that most cracks are concentrated in the central area of the west layby enlargement, with a higher density in contrast to the diameter-variant area in non-VCP sections. This suggests that the strength and stiffness of the lining (due to the tunnel configuration) increased less around the central area of the layby tunnel, resulting in a greater subsequent increase in tunnel internal forces and deformation.

Figure 19(b) and (c) demonstrates that the area surrounding the VCP in the layby tunnel exhibits minimal cracking, in contrast to the other side of the same bore, as shown in Fig. 19(a) and (d), respectively. This phenomenon may be attributed to the pushback from the VCP at the layby-VCP conjunction area, which results in strengthening and stiffening in the lateral compression responses at the layby-VCP connection, as illustrated in Fig. 17(b).

Meanwhile, the defect distribution patterns give evidence to infer the tunnel's deterioration mode. It's noted that NB tunnel linings generally have more cracks than SB ones. The underlying mechanism may be attributed to the presence of maintenance tunnel, which weakened the ground arching [33] for NB lining as illustrated in Fig. 20. In Fig. 19(a), most of the lining cracks are vertical cracks while some as diagonal cracks [34], in line with previous findings that vertical cracks are the dominant type of tunnel cracks [35,36]. Furthermore, the west linings of both NB and SB tunnels (Fig. 19(a) and (c)) exhibit a higher crack density than the east linings (Fig. 19(b) and (d)). These vertical crack distributions in the west & east linings are most likely associated with the longitudinal tunnel bending deformation mode [20]. Fig. 20 illustrates that the curved tunnel geometry results in tension on the east side of the linings of both the NB and SB tunnels. The red, yellow and green arrows indicate the inferred relative density of crack defects on the concrete surface, which is high, middle and low occurrence respectively.

In summary, the crack distribution can be employed to infer or validate the tunnel deformation mode. Firstly, the headwall effect, the layby effect and the VCP effect have been validated. The vicinity of these reinforced structures is more resistant to cracks. Also, the tunnel longitudinal bending of the tunnel and the structure of maintenance tunnel seems to cooperatively trigger the difference in crack density between linings. Cracks appears to be more prevalent in the NB than in the SB, and more in the west linings than the east linings. Additionally, the observed asymmetric crack distribution may also be attributed to the combined effect of the tunnel structure configuration, local geological variability, a slightly earlier construction time of NB than SB and VCP, and other factors. Further research would necessitate a more comprehensive understanding of these factors to confirm their role in this observed tunnel defect distribution.

4.2.4. *Quantification of water leakage*

The data regarding the number and size of water leakage are presented in Fig. 19 with yellow box and Table 6 with the dimensions. In the tunnel sidewall inspection scenario, the water leakage is either from horizontal cracks or the blocked drainage. They can be identified by the width of the leakage (length in the horizontal direction of the tunnel). The crack-oriented leakage has a greater width, while the drainage-oriented width is almost the same as the drainage's. The length of the leakage reflects its severity since the last cleaning of the tunnel lining. A greater length along the tunnel surface indicates a greater volume of leakage.

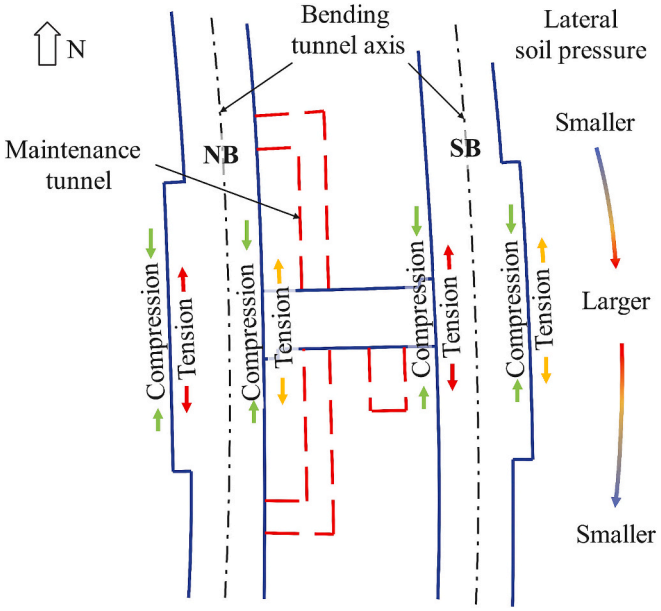


Fig. 20. Schematic of the tunnel construction plan



(a) From lining cracks (b) From positive drains (c) Through construction joints

Fig. 21. Water leakage example in orthomosaics

Regarding water leakage in DPT, maintenance records indicate greater hydraulic deterioration in the northern part of the tunnel, as exemplified by the orthomosaics in Fig. 21. Water leakage penetrates the tunnel lining through various channels in the form of seepage, such as positive drains, construction joints, and lining cracks. The leakage of groundwater into the tunnel comes with intruding dark ground particles, indicating ground erosion and/or weathering behind tunnel lining [20]. The presence of progressive water leakage, together with the indicative ground erosion/weathering, leads to an increased humidity inside tunnel, an acceleration of deterioration of tunnel lining materials and soil behind, and an increase in ground pressure acting on tunnel lining. This means that an increasing tunnel internal forces and deformation is imminent. In the long term, the propagation of concrete cracks aggravates water leakage (i.e., a growing amount of water leakage into the tunnels), and in turn, the development of water infiltration also exacerbates lining cracking, contributing to an increasing tunnel deformation [20].

In summary, the quantification of lining cracks shows that diameter-variant area sees scarce number of cracks due to its higher stiffness than the surrounding areas, the concentration of cracks in the middle of NB west lining is associated with the VCP effect, and the non-presence of cracks around the layby-VCP conjunction area could be attributed to the strengthening/stiffening in lateral compression responses at the conjunction. In comparison, the quantification of water leakage shows no clear pattern of distribution within the inspected area, but such leakage mainly comes from construction joints, cracks and drains.

5. Discussion

This study presents an automated UAV-based inspection and assessment methodology for a cross-passage twin tunnel section of the Dublin Port Tunnel, focusing on its structural deformation and surface defect analysis. The UAV-based inspection method, supported by DSMs and orthomosaics, successfully identifies key tunnel deformation patterns and tunnel deteriorations. The findings contribute to a deeper understanding of the interactions between tunnel geometry, structural stiffness, and tunnel deteriorations.

One of the significant observations in this study is the impact of tunnel geometry on its structural deformation. The results confirm that diameter-variant sections, particularly those near the headwall, exhibit minimal deformation due to increased structural stiffness. The layby section, in contrast, shows a tendency for inward compression towards the tunnel centreline, aligning with the expected twin tunnel interaction effect. Additionally, the reduced deformation observed at the vehicle cross passage section supports previous findings that VCP structures provide lateral pushback, reducing compression effects in the adjacent lining sections.

The UAV-based assessment also highlights distinct patterns in lining defect distribution. The observed cracks predominantly follow a vertical and diagonal orientation, with higher crack densities recorded in the west linings of the tunnel section. This asymmetric defect distribution suggests that differential structural stiffness and tunnel longitudinal bending play a critical role in crack initiation and propagation. Moreover, the presence of an additional maintenance tunnel in the NB bore likely weakens ground arching effects, leading to increased structural stress and defect formation. In contrast, water leakage does not exhibit a strong correlation with tunnel geometry, and instead it occurs at construction joints, lining cracks, and drainage points. The presence of seepage with dark ground particles suggests progressive ground erosion behind the tunnel lining, which could accelerate structural deterioration over time, which aligns with previous monitoring data and reinforces the importance of early detection and preventive maintenance strategies.

While this study demonstrates the effectiveness of UAV-based tunnel inspection and assessment, certain limitations remain. The spatial resolution of the UAV-derived DSMs is in the centimetre range, limiting their precision in detecting subtle deformations that may require millimetre-scale accuracy. Future studies could integrate UAV inspections with techniques like terrestrial laser scanning to enhance accuracy. In addition, machine learning-based defect recognition could further automate the analysis of crack propagation and defect classification, improving the reliability and efficiency of such UAV-based monitoring. Overall, the findings reinforce the viability of UAVs as a cost-effective and adaptive tool for tunnel inspections, particularly in geometrically complex environments where traditional inspection methods face challenges. The insights gained from this study could contribute to a more comprehensive understanding of tunnel deformation and deterioration mechanisms, aiding in the development of more effective maintenance and rehabilitation strategies for underground tunnel infrastructure.

6. Conclusions

This research has undertaken an automated inspection of a cross-passage twin tunnel section with layby enlargement. It has developed and validated an automated UAV-based inspection method for assessing tunnel structural health, demonstrating its effectiveness in a geometrically complex cross-passage twin tunnel section of DPT. The proposed method uses UAV-captured images for assessment of structural health conditions, particularly about structural deformation and surface defects. This study successfully applies a workflow for data interpretation, which uses DSMs to analyse tunnel deformation and orthomosaics for tunnel lining defects quantification. This method outperforms conventional techniques in improved accuracy and efficiency, with the latter often relying on manual processes susceptible to human errors. In summary, the primary discoveries and contributions of this paper can be

listed as follows:

(1) The proposed automated image acquisition methodology PMPP-SDI in UAV control was validated during the inspection task in the diameter-variant cross-passage twin tunnel section, demonstrating the method's efficacy across a comprehensive spectrum of inspection conditions. The accuracy of lateral and height control is 0.6 m and 0.1 m, respectively.
(2) The comprehensive image processing workflow enables the extraction of tunnel configuration data from digital surface models (DSMs) and the identification of tunnel lining defects from orthomosaics. A comparison between the profiles in DSMs and the as-built lining profiles showed that (*i*) the deformation observed at the headwall was less significant than in other sections due to its higher stiffness, which limits the development of cross-sectional deformation; (ii) the layby sections were all compressed towards the twin tunnel centreline due to the effect of twin tunnel interaction; (iii) the fitted VCP section experienced a smaller degree of compression compared to other sections (i.e., Section D, Section E and Section F), which corresponds to the VCP effect (horizontal pushback from VCP).
(3) The orthomosaics revealed two main types of tunnel defects: lining cracks and water leakage. The quantification of lining cracks demonstrates headwall effect, that is, fewer cracks develop in diameter-variant areas due to the higher structural stiffness because of the thickened headwall. The layby effect exhibits a higher density of cracks in the central area of the layby enlargement than in the other layby areas due to less strengthening in the area. The VCP effect shows an absence of cracks in the NB east lining and SB west lining around of the layby-VCP conjunction area, in comparison to the opposite side of the same tunnel (NB west lining and SB east lining) due to strengthening/stiffening in lateral compression responses at layby-VCP connection. The vertical cracks are dominant in the west lining of NB, and they are likely to be associated with the differential deformation of the tunnel section induced by longitudinal bending. The greater number of cracks in NB linings than those in SB linings might be related to the additional maintenance tunnel that weakens the ground arching.
(4) In contrast, the quantification of water leakage shows no discernible pattern of distribution within the inspected area. However, it was observed that such water leakage is primarily attributable to construction joints, lining cracks and tunnel drains.

While this study presents an effective UAV-based method for automatic tunnel inspection, it faces certain limitations. The spatial resolution of the UAV-derived DSMs is in the centimetre range, limiting the precision needed for detecting subtle deformations, which typically require mm-level accuracy. In addition, environmental factors such as noise clusters during image acquisition, poor lighting conditions, and obstruction by tunnel elements may lead to inaccuracies in model reconstruction. The UAV's ability to capture data in certain challenging environments could be further enhanced through calibration.

Therefore, future studies could focus on enhancing the UAV's inspection accuracy through multi-source data fusion, such as integrating other technologies like terrestrial laser scanning. This would allow for more accurate measurement of deformations and quantification of minor defects that might be missed at the current level of resolution. Another area that future research could explore is to integrate advanced machine learning algorithms for automated defect recognition and classification. This would not only increase the efficiency of data processing but also improve the reliability of identifying subtle defects such as minor cracks or water seepage. The approach presented in this paper could also be applied to other complex tunnel systems, such as those with intricate intersections or multiple parallel bores, where traditional methods face limitations. Expanding the application of UAVs to these tunnels would provide a cost-effective and adaptive solution, especially in tunnels located in regions with difficult access or hazardous conditions.

CRediT authorship contribution statement

Ran Zhang: Writing – review & editing, Writing – original draft, Visualization, Methodology, Investigation, Formal analysis, Data curation, Conceptualization. **Chao Wang:** Writing – review & editing, Validation, Methodology, Investigation, Formal analysis, Conceptualization. **Zili Li:** Writing – review & editing, Validation, Supervision, Resources, Project administration, Funding acquisition.

Declaration of competing interest

The authors declare the following financial interests/personal relationships which may be considered as potential competing interests:

Ran zhang reports financial support was provided by China Scholarship Council.

Acknowledgement

Ran Zhang acknowledges the support from the China Scholarship Council; Chao Wang would like to thank the joint funding from the Irish Centre for Research in Applied Geoscience of Science Foundation Ireland and Transport Infrastructure Ireland; The authors acknowledge the support from Science Foundation Ireland for a research grant under the Frontiers for the Future Programme [grant number: 21/FFP-P/10090].

Appendix A

Figure A describes the UAV inspection strategies in three scenarios of DPT for surface defect identification:

Scenario A involves small diameter, well lit, and straight tunnels. These tunnels allow the UAV to rely on visual navigation to move along the axis.

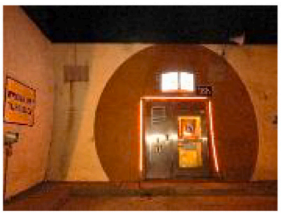
Scenario B includes tunnel sections with slight diameter changes, uniform large tunnel sections, or weak lighting conditions. Here, dual spotlights provide limited confidence in front and back distance readings, so the UAV flies at a fixed distance parallel to the wall, making small adjustments to its yaw.

Scenario C includes tunnels with large diameter changes and total darkness. Here the UAV doesn't capture additional surface details of distant structures as they are of less inspection interest. The UAV maintains its flight path in a fixed direction, without adjusting its lateral position or yaw.



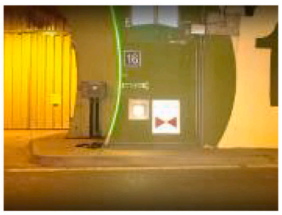
(1a) Scenario A:

A slightly curved surface



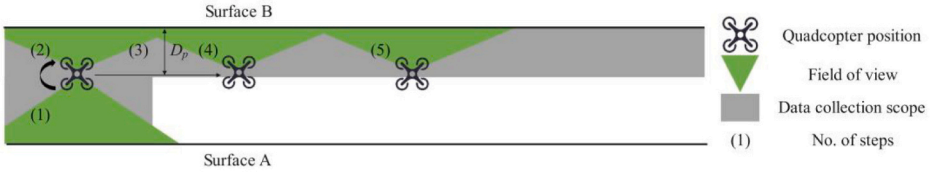
(1b) Scenario B:

Small tunnel diameter change

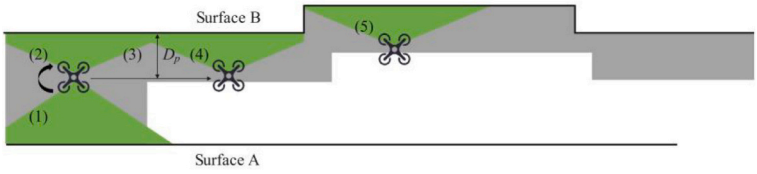


(1c) Scenario C:

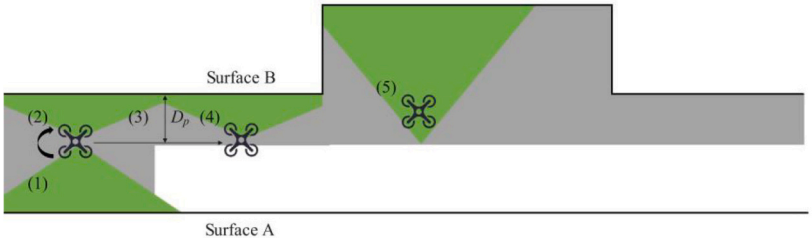
Large tunnel diameter change



(2a) Scenario A: UAV moves along a straight routine parallel to the tunnel axis.



(2b) Scenario B: UAV moves along the tunnel side wall.



(2c) Scenario C: UAV moves along the original route.

Fig. A. Three flying strategies in the PMPP-SDI method for UAV inspection varying structural and luminance (see [11] for details).

Data availability

Data will be made available on request.

References

[1] Centre d'Études des Tunnels, Road Tunnel Civil Engineering Inspection Guide Book 2: Catalogue of Deteriorations, Bron, France, Accessed: Jun. 04, 2023. [Online]. Available: https://www.cetu.developpement-durable.gouv.fr/IMG/pdf/catalogue_of_deteriorations.pdf, 2015.

[2] R. Montero, J.G. Victores, S. Martínez, A. Jardón, C. Balaguer, Past, present and future of robotic tunnel inspection, Autom. Constr. 59 (2015) 99–112, https://doi.org/10.1016/j.autcon.2015.02.003.

[3] A. Ouyang, V. Di Murro, M. Cull, R. Cunningham, J. A. Osborne, and Z. Li, 'Automated pixel-level crack monitoring system for large-scale underground infrastructure – a case study at CERN', Tunnelling and Underground Space Technology, vol. 140, p. 105310, Oct. 2023, doi: https://doi.org/10.1016/j.tust.2023.105310.

[4] Y.H. Lee, R. Kumar, J.M. Benz, H. McGee-Hilbert, G. Hollinger, C.J. Palmer, Autonomous Inspection of Geologic Repositories: Current State of the Art and Future Directions, Pacific Northwest National Lab. (PNNL), Richland, WA (United States), Oct. 2020, https://doi.org/10.2172/1824167. PNNL-30566.

[5] R.M. Turner, M.M. MacLaughlin, S.R. Iverson, Identifying and mapping potentially adverse discontinuities in underground excavations using thermal and multispectral UAV imagery, Eng. Geol. 266 (2020) 105470, https://doi.org/10.1016/j.enggeo.2019.105470.

[6] T. McDonald, M. Robinson, G.Y. Tian, Developments in 3D visualisation of the rail tunnel subsurface for inspection and monitoring, Appl. Sci. 12 (22) (2022), https://doi.org/10.3390/app122211310. Art. no. 22.

[7] R. Zhang, G. Hao, K. Zhang, Z. Li, Unmanned aerial vehicle navigation in underground structure inspection: a review, Geol. J. 58 (6) (2023) 2454–2472, https://doi.org/10.1002/gj.4763.

[8] E.A. Russell, M.M. MacLaughlin, R.M. Turner, UAV-Based Geotechnical Modeling and Mapping of an Inaccessible Underground Site, in: Presented at the 52nd U.S. Rock Mechanics/Geomechanics Symposium, OnePetro, 2018. Accessed: May 21, 2024. [Online].

[9] S. P, A. Varughese, H. Dev, N. Kumar, Estimation of Q-value and deformation modulus of rock mass using seismic refraction survey for hydropower project, Water Energy Intern. 62 (2019) 48, e-ISSN: 0974–4711, e-ISSN: 0974–4711.

[10] F. Azhari, S. Kiely, C. Sennersten, C. Lindley, M. Matuszak, S. Hogwood, A comparison of sensors for underground void mapping by unmanned aerial vehicles, Austral. Centre Geomechan. (2017), https://doi.org/10.36487/ACG_rep/1710_33_Sennersten.

[11] R. Zhang, G. Hao, K. Zhang, Z. Li, Reactive UAV-based automatic tunnel surface defect inspection with a field test, Autom. Constr. 163 (2024) 105424, https://doi.org/10.1016/j.autcon.2024.105424.
[12] B.A. McCabe, T.L.L. Orr, C.C. Reilly, B.G. Curran, Settlement trough parameters for tunnels in Irish glacial tills, Tunn. Undergr. Space Technol. 27 (1) (2012) 1–12, https://doi.org/10.1016/j.tust.2011.06.002.
[13] M. Petrlík, T. Báča, D. Heřt, M. Vrba, T. Krajník, M. Saska, A robust UAV system for operations in a constrained environment, IEEE Robot. Automat. Lett. 5 (2) (2020) 2169–2176, https://doi.org/10.1109/LRA.2020.2970980.
[14] M.Y. Arafat, M.M. Alam, S. Moh, Vision-based navigation techniques for unmanned aerial vehicles: review and challenges, Drones 7 (2) (2023), https://doi.org/10.3390/drones7020089. Art. no. 2.
[15] D. Kominiak, S.S. Mansouri, C. Kanellakis, G. Nikolakopoulos, MAV Development Towards Navigation in Unknown and Dark Mining Tunnels, in: 2020 28th Mediterranean Conference on Control and Automation (MED), 2020, pp. 1015–1020, https://doi.org/10.1109/MED48518.2020.9183142.
[16] C.H. Tan, M. Ng, D.S.B. Shaiful, S.K.H. Win, W.J. Ang, S.K. Yeung, H.B. Lim, M. N. Do, S. Foong, A smart unmanned aerial vehicle (UAV) based imaging system for inspection of deep hazardous tunnels, Water Pract. Technol. 13 (4) (2018) 991–1000, https://doi.org/10.2166/wpt.2018.105.
[17] M.A.A. Sourav, M. Mahedi, H. Ceylan, S. Kim, C. Brooks, D. Peshkin, R. Dobson, M. Brynick, Evaluation of small Uncrewed aircraft systems data in airfield pavement crack detection and rating, Transp. Res. Rec. 2677 (1) (2023) 653–668, https://doi.org/10.1177/03611981221101030.
[18] N. Mullally, Dublin Port Tunnel Project, Accessed: Oct. 04, 2023. [Online]. Available: https://dublintunnel.ie/wp-content/uploads/pdf/dublin-tunnel-press-pack.pdf.
[19] A. Gillarduzzi, Investigating property damage along Dublin port tunnel alignment, Proceed. Inst. Civ. Eng. - Forens. Eng. 167 (3) (2014) 119–130, https://doi.org/10.1680/feng.13.00024.
[20] C. Wang, M. Friedman, Z. Li, Monitoring and assessment of a cross-passage twin tunnel long-term performance using wireless sensor network, Can. Geotech. J. (2023), https://doi.org/10.1139/cgj-2022-0224.
[21] M.A.A. Sourav, H. Ceylan, C. Brooks, D. Peshkin, S. Kim, R. Dobson, A. Jenkins, C. Cook, Practical Lessons Learned from Planning, Collecting, Processing, and Analyzing Small Unmanned Aircraft System Data for Airfield Pavement Inspection, DOT/FAA/TC-22/48, 2022, https://doi.org/10.21949/1524519.
[22] S.I. Jiménez-Jiménez, W. Ojeda-Bustamante, M. de J. Marcial-Pablo, J. Enciso, Digital terrain models generated with low-cost UAV photogrammetry: methodology and accuracy, ISPRS Int. J. Geo Inf. 10 (5) (2021), https://doi.org/10.3390/ijgi10050285. Art. no. 5.
[23] S. Agnisarman, S. Lopes, K. Chalil Madathil, K. Piratla, A. Gramopadhye, A survey of automation-enabled human-in-the-loop systems for infrastructure visual inspection, Autom. Constr. 97 (2019) 52–76, https://doi.org/10.1016/j.autcon.2018.10.019.
[24] Z. Li, K. Soga, P. Wright, Long-term performance of cast-iron tunnel cross passage in London clay, Tunn. Undergr. Space Technol. 50 (2015) 152–170, https://doi.org/10.1016/j.tust.2015.07.005.
[25] K. Loupos, A.D. Doulamis, C. Stentoumis, E. Protopapadakis, K. Makantasis, N. D. Doulamis, A. Amditis, P. Chrobocinski, J. Victores, R. Montero, E. Menendez, C. Balaguer, R. Lopez, M. Cantero, R. Navarro, A. Roncaglia, L. Belsito, S. Camarinopoulos, N. Komodakis, P. Singh, Autonomous robotic system for tunnel structural inspection and assessment, Int. J. Intell. Robot. Appl. 2 (1) (2018) 43–66, https://doi.org/10.1007/s41315-017-0031-9.
[26] C. Yi, D. Lu, Q. Xie, S. Liu, H. Li, M. Wei, J. Wang, Hierarchical tunnel modeling from 3D raw LiDAR point cloud, Comput. Aided Des. 114 (2019) 143–154, https://doi.org/10.1016/j.cad.2019.05.033.
[27] Z. Gao, F. Li, Y. Liu, T. Cheng, Y. Su, Z. Fang, M. Yang, Y. Li, J. Yu, Q. Zhang, Tunnel contour detection during construction based on digital image correlation, Opt. Lasers Eng. 126 (2020) 105879, https://doi.org/10.1016/j.optlaseng.2019.105879.
[28] M. Lei, L. Liu, C. Shi, Y. Tan, Y. Lin, W. Wang, A novel tunnel-lining crack recognition system based on digital image technology, Tunn. Undergr. Space Technol. 108 (2021) 103724, https://doi.org/10.1016/j.tust.2020.103724.
[29] R. A. Pietersen, 'Automated Method for Airfield Pavement Condition Index Determination', Master Theses, Massachusetts Institute of Technology. [Online]. Available: http://rightsstatements.org/page/InC-EDU/1.0/.
[30] M.A.A. Sourav, H. Ceylan, C. Brooks, D. Peshkin, S. Kim, R. Dobson, C. Cook, M. Mahedi, O. Brouillette, Small Unmanned Aircraft System for Pavement Inspection: Task 4—Execute the Field Demonstration Plan and Analyze the Collected Data, 2022, https://doi.org/10.21949/1524511. DOT/FAA/TC-22/35.
[31] X. Peng, X. Zhong, C. Zhao, A. Chen, T. Zhang, A UAV-based machine vision method for bridge crack recognition and width quantification through hybrid feature learning, Constr. Build. Mater. 299 (2021) 123896, https://doi.org/10.1016/j.conbuildmat.2021.123896.
[32] S. Bohari, A. Amran, N. Mohd Zaki, S. Suhaimi, A.R. Abdul Rasam, Accuracy assessment of detecting cracks on Concrete Wall at different distances using unmanned autonomous vehicle (UAV) images, IOP Confer. Ser.: Earth Environ. Sci. 620 (2021) 012005, https://doi.org/10.1088/1755-1315/620/1/012005.
[33] K. Soga, R.G. Laver, Z. Li, Long-term tunnel behaviour and ground movements after tunnelling in clayey soils, Underground Space 2 (3) (2017) 149–167, https://doi.org/10.1016/j.undsp.2017.08.001.
[34] D.O. Brien, J. Andrew Osborne, E. Perez-Duenas, R. Cunningham, Z. Li, Automated crack classification for the CERN underground tunnel infrastructure using deep learning, Tunn. Undergr. Space Technol. 131 (2023) 104668, https://doi.org/10.1016/j.tust.2022.104668.
[35] H. Wang, H. Huang, Y. Feng, D. Zhang, Characterization of crack and leakage defects of concrete linings of road tunnels in China, ASCE-ASME J. Risk Uncert. Eng. Syst. Part A: Civ. Eng. 4 (4) (2018) 04018041, https://doi.org/10.1061/AJRUA6.0000989.
[36] G. Xu, C. He, Z. Chen, C. Liu, B. Wang, Y. Zou, Mechanical behavior of secondary tunnel lining with longitudinal crack, Eng. Fail. Anal. 113 (2020) 104543, https://doi.org/10.1016/j.engfailanal.2020.104543.